Journal of Magnetism and Magnetic Materials 392 (2015) 27–41

Contents lists available at ScienceDirect

Journal of Magnetism and Magnetic Materials

journal homepage: www.elsevier.com/locate/jmmm

# Structural, magnetic and electronic properties on the Li-doped manganites

A.M. Ahmed [a], G. Papavassiliou [b], H.F. Mohamed [a,*], E.M.M. Ibrahim [a]

[a] Physics Department, Faculty of Science, Sohag University, 82524 Sohag, Egypt
[b] Institute of Materials Science, NCSR Demokritos, Aghia Paraskevi, Greece

ARTICLE INFO

*Article history:*
Received 22 March 2015
Received in revised form
30 April 2015
Accepted 4 May 2015
Available online 6 May 2015

*Keywords:*
Composite materials
Heat treatment
Electron microscopy
Electrical characterization
Magnetometer
Rietveld analysis

ABSTRACT

We present results of a comprehensive investigation of the structural, frequency dependent ac susceptibility, dc magnetization, magnetoresistance and thermoelectric power measurements on polycrystalline samples of $La_{1-x}Li_xMnO_3$ ($0.05 \le x \le 0.30$). All samples undergo ferromagnetic to paramagnetic transition and metal to semiconductor transition. A cusp in the zero field-cooled in dc magnetization and a frequency-dependent peak in the ac susceptibility reveal the glassy behaviors. The out of phase component of the ac susceptibility shows frequency-dependent peaks below the Curie temperature (indicative of glassy behavior) which have previously been interpreted in terms of freezing of clusters. The grain boundaries play a dominant role in the conduction process. The framework of the magnon and phonon drag concept analyzed thermoelectric power data at low temperature, while small polaron conduction mechanism explained thermoelectric power data at high temperature. It has been found that the percolation threshold sample is $x=0.10$, so the author's point of view refers to make spot on this sample in the future works.



## 1. Introduction

The magnetoresistance (MR) phenomenon [1] has attained interest from scientists due to their industrial applications in magnetic, magnetoelectronic, photonic devices, infrared detector, as well as spintronic technology.

The $R_{1-x}A_xMnO_3$ compounds (R=rare earth and A=divalent alkali) were extensively studied for their significant magnetic behaviors [2–4]. The undoped compound $LaMnO_3$ ($x=0$) is an antiferromagnetic semiconductor (AFS) which evolves to a ferromagnetic metal (FMM) when a mixed $Mn^{3+}/Mn^{4+}$ valency is induced by the $R^{3+}/A^{2+}$ substitution. This interpreted by the double exchange theory (DE), where the carrier spins are aligned and hope from one Mn-site to the other through Mn–O–Mn without change in their spin orientation [4]. The $Mn^{3+}/Mn^{4+}$ ratio can play a large role in the different interactions such as double exchange (DE) [5], superexchange (SE) and coulomb interaction (CI) among Mn ion. The relative change in $Mn^{3+}/Mn^{4+}$ is due to a competition between the double exchange (DE) ferromagnetism (FM) and the superexchange (SE) antiferromagnetism (AFM), as a result of a homogenous or inhomogeneous distribution of electron density which leads to phase transition [6,7–9] and the coexistence different magnetic phases in manganites [7–9].

The other parameter can effect on the magnetic and electric behavior of the materials is the average size of the A-site cation.

Relieve of incorporates the different sized A-site cation in perovskite structure make it available to design a verity of manganites, giving a wide range of magnetotransport properties. A-site disorder caused by occupying the A-site with different sized ion, its importance (variance $\sigma^2=\Sigma i\ x_i r_i^{\ 2}-\langle r_A\rangle$) for the magnetic and electrical transitions is well-understood [10].

The basic physics of doped manganites is not only dependent on the DE interaction but there is other mechanism such as the formation of the small polaron in the paramagnetic–semiconducting (PMS) phase [11].

The semiconducting behavior explained by the polaron formation [12] and polaronic hopping conduction mechanism. In these magnetic manganites such a competition between AFM and FM favors the spin-glass (SG) state at low temperature.

The thermoelectric power (TEP) is a crucial tool to inspect important properties of the polycrystalline samples [13,14] including the type of the dominant carrier [15]. Noteworthy, in the transition metal oxide, various mechanisms such as diffusion, phonon drag, or magnon drag can influence the TEP [16]. However,

* Corresponding author. Fax: +20 934601159
*E-mail addresses:* h.fathy@science.sohag.edu.eg, dr_Hanyfathy@yahoo.com (H.F. Mohamed).

http://dx.doi.org/10.1016/j.jmmm.2015.05.004
0304-8853/

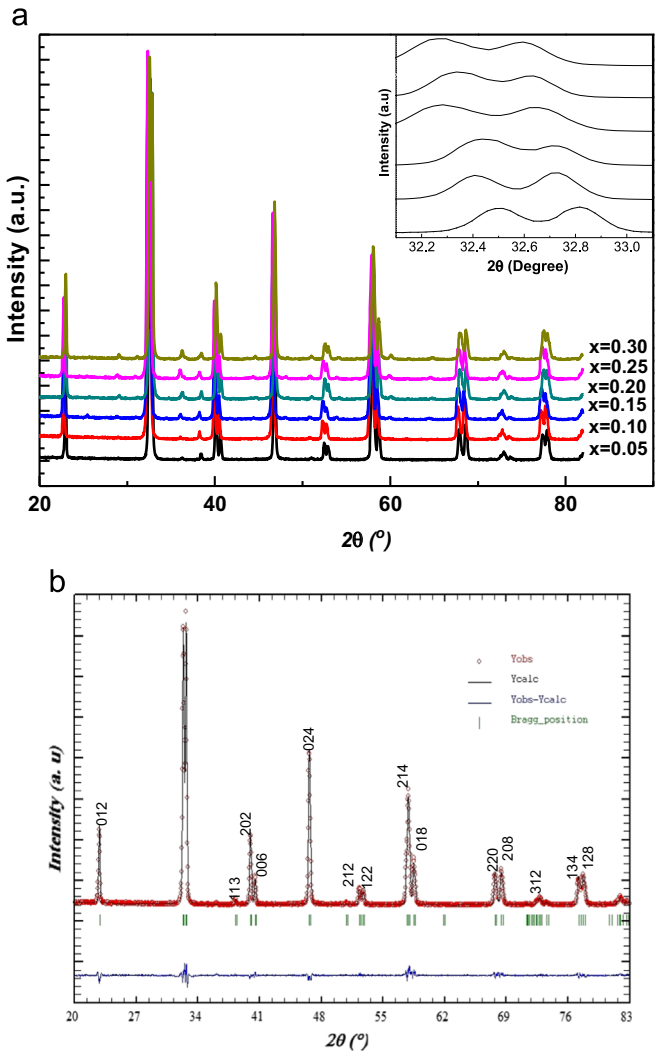


**Fig. 1.** XRD diffraction patterns for $La_{1-x}Li_xMnO_3$ ($x$=0.05, 0.10, 0.15, 0.20, 0.25 and 0.30), the inset shows the variation of peak shape with doping for the most intense peak. (b) Rietveld refined patter of the $La_{0.95}Li_{0.05}MnO_3$ sample.

deep interpretation of the temperature dependence of Seebeck coefficient [$S(T)$] is rarely reported [17–19].

This work presents a study on the effect of Li doping on the magnetic, electrical, magnetoresistance and thermoelectric properties of $LaMnO_3$. Through magnetization (dc and ac), resistivity (with and without applied magnetic field) and Seebeck coefficient measurements, we present a comprehensive configuration of the empirical behavior of the compositions under study.

## 2. Experimental

Set of $La_{1-x}Li_xMnO_3$ samples with $x$= 0.05, 0.10, 0.15, 0.20, 0.25 and 0.30 were prepared by a conventional solid-state reaction method. Specifically, amounts of $La_2O_3$, $Li_2CO_3$ and $MnO_2$ powders (99.99% purity) were mixed together according to the stoichiometric ratios and then ground thoroughly. Each mixture was pressed into small pellets under pressure 2ton/cm$^2$, subsequently, the pellets were calcined at 1273 K for 24 h. After cooling to room temperature, they were reground and again pressed into pellets and sintered at 1373 K for 48 h. The x-ray diffraction (XRD) investigation was carried out at room temperature using Brucker (Axs-D8Advance) diffractometer with $CuK_\alpha$ radiation ($\lambda$=1.5406 Å). The dc magnetic properties were studied using a superconducting quantum interference device (SQUID) magnetometer (Quantum Design) and the ac susceptibility was measured using the magnetic option of the physical property measurement system (PPMS) of Quantum Design. The resistivity was measured as a function of temperature using the standard four-point method. The thermoelectric power measurements were carried out by means of a home-built setup published in our previous work [20–22].

## 3. Results and discussion

### 3.1. Structural properties

Fig. 1 shows the x-ray diffraction patterns of the samples determined at room temperature. The data imply that the samples of $x \leq 0.10$ are single rhombohedral phase with space group $R\bar{3}c$,

**Table 1**
Rietveld refined of $La_{1-x}Li_xMnO_3$ ($x$=0.05, 0.10, 0.15, 0.20, 0.25 and 0.30) manganite system (with $R\bar{3}c$ space group) at room temperature.

| *X* | 0.05 | 0.1 | 0.15 | 0.2 | 0.25 | 0.3 |
|---|---|---|---|---|---|---|
| **Cell parameter** | | | | | | |
| $a$ (Å)=$b$ (Å) | 5.5308 | 5.5266 | 5.5258 | 5.5247 | 5.5243 | 5.5218 |
| $c$ (Å) | 13.3579 | 13.3559 | 13.3526 | 13.3508 | 13.3507 | 13.3462 |
| Volume (Å$^3$) | 353.8708 | 353.3873 | 353.0912 | 352.9 | 352.8492 | 352.4117 |
| **Bond length** | | | | | | |
| La/Li–O | 2.666 | 2.6635 | 2.6625 | 2.6624 | 2.6618 | 2.6593 |
| Mn–O (Å) | 1.9648 | 1.9637 | 1.9649 | 1.965 | 1.9655 | 1.9656 |
| **Bond angle** | | | | | | |
| Mn–O–Mn (deg) | 163.9 | 164 | 163.61 | 163.54 | 163.48 | 163.22 |
| O($x$) | 0.4505 | 0.4491 | 0.4489 | 0.4493 | 0.4481 | 0.4504 |
| $Mn^{4+}$% | 10.0204 | 20.006 | 29.9994 | 40.0036 | 50 | 59.9988 |
| $\Delta$ | 0.098 | 0.067 | 0.037 | 0.119 | -0.001 | 0.066 |
| Tolerance factor ($t_{calc}$ ) | 0.9527 | 0.9511 | 0.9496 | 0.948 | 0.9464 | 0.9441 |
| Tolerance factor ($t_{obs}$) | 0.9595 | 0.9591 | 0.9582 | 0.9581 | 0.9576 | 0.9567 |
| $\sigma^2$ ( Å$^2$) | 0.0076 | 0.0144 | 0.0204 | 0.0256 | 0.03 | 0.0336 |
| $\langle r_A \rangle$ (Å) | 1.2660 | 1.2635 | 1.2625 | 1.2624 | 1.2618 | 1.2593 |
| average crystallite size $L$ (nm)$_{XRD}$ | 54.47 | 69.32 | 57.64 | 55.58 | 54.47 | 49.33 |
| ***R*-factor (%)** | | | | | | |
| $R_p$ | 9.88 | 10.7 | 18.1 | 17 | 16.9 | 17.8 |
| $R_{wp}$ | 13.7 | 14.3 | 21.7 | 20.8 | 20.2 | 22.3 |
| $R_f$ | 3.64 | 5.46 | 7.83 | 8.95 | 6.19 | 9.2 |
| $R_{Bragg}$ | 3.4 | 3.47 | 6.53 | 6.74 | 6.99 | 7.11 |
| Goodness of fit indicator $\chi$ | 1.387 | 1.336 | 1.199 | 1.224 | 1.195 | 1.253 |

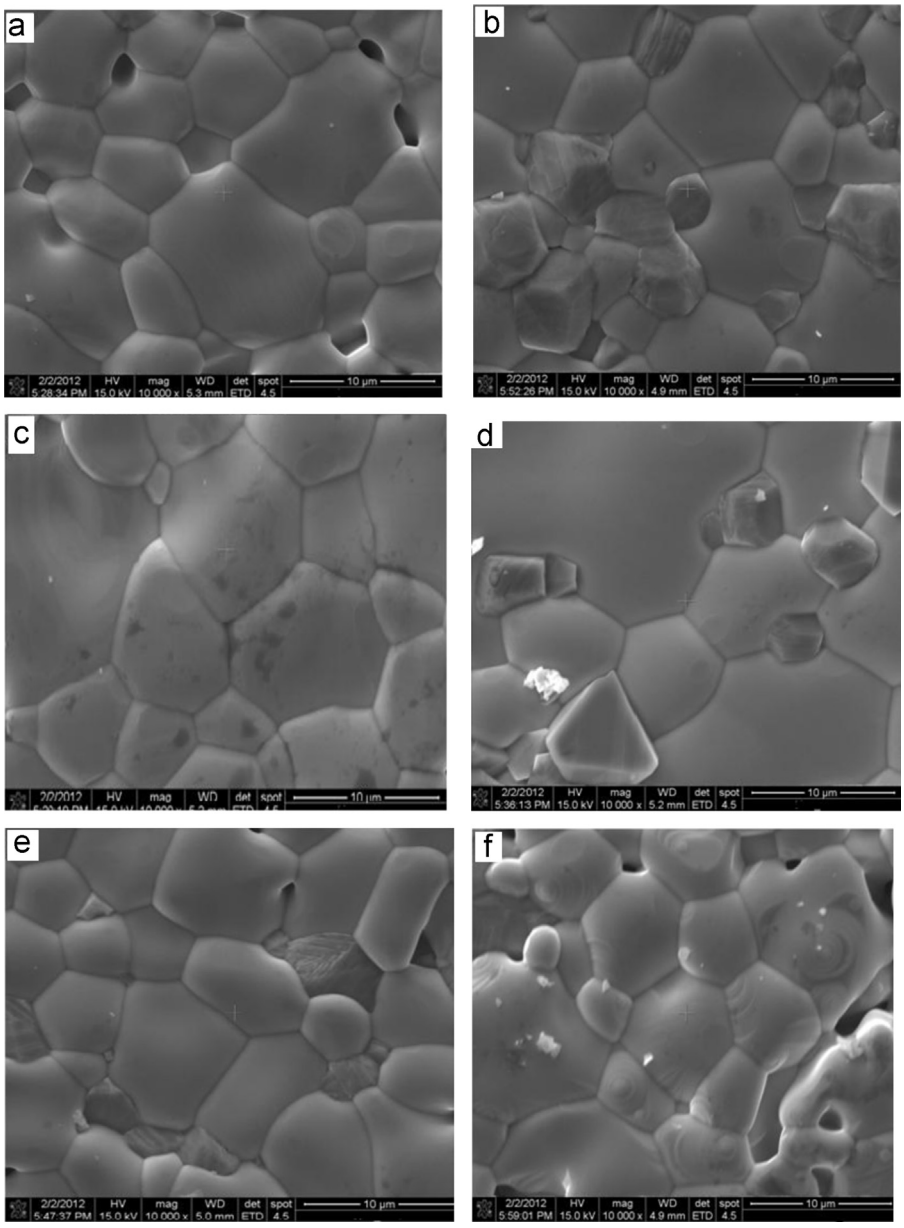


**Fig. 2.** Scanning electron micrographs of of $La_{1-x}Li_xMnO_3$ ($a-x=0.05$, $b-x=0.10$, $c-x=0.15$, $d-x=0.20$, $e-x=0.25$, and $f-x=0.30$) manganites.

where La/Li atoms are located at 6 a (0, 0, 0.25), Mn at 6b (0, 0, 0) and O at 18e ($x$, 0, 0.25) Wyckoff positions. Note that no peaks of impurities or other phases could be detected. The samples with ($0.15 \leq x \leq 0.3$) are close to single phase with minor amount of $Mn_3O_4$ impurity. Noteworthy, Shih et al. [23] obtained similar results, and they imputed the appearance of the impurity phases to limitation of Li solubility in La sub-lattice. Such limitation causes mismatch in the valence and ionic radius between Li and La. Similarly, Rao et al. [24] reported about appearance of similar type of impurity phase (with ratio 5%) in Na-doped $LaMnO_3$ sample and they confirm that it has no influence on any of the physical properties. The gradual change in the shape of split peaks (110) and (104) (see inset of Fig. 1(a)) suggests onset of the orthorhombic phase [25].

Stander Rietveld refinement technique was utilized for refining the experimental data and calculating the cell parameters of all samples and the data are presented in Table 1. A typical plot of XRD pattern of x= 0.05 with its Rietveld refined one, including the difference between observed and calculated patterns are shown in Fig. 1(b) as an example. Generally, one can observe that the lattice parameters and the unit-cell volume decrease as the lithium content increases. This shrinkage of the lattice with Li doping is due to two factors: firstly, the ionic radius of Li (0.092 nm) is much smaller than that of La ion (0.136 nm) [26], secondly, increasing the Li content increases $Mn^{4+}$ ion, which has smaller (ionic radii, 0.53 Å) than the $Mn^{3+}$ ion (ionic radii, 0.645 Å) [26]. Presence of smaller cations in the B sublattice of the $ABO_3$ perovskite is responsible also for the lattice distortion because of the mismatch between the sizes of ions and the interstices occupied by them in the perovskite lattice. The lattice distortion is represented by the tolerance factor $t_{calc,obs.}=(r_A+r_O)/\sqrt{2}(r_{Mn}+r_O)=d_{A-O}/\sqrt{2}d_{B-O}$ (where $r_A$, $r_{Mn}$, and $r_O$, are the ionic radii for A-site, Mn-site and oxygen ion, respectively). If $t$ is close to one, the cubic perovskite structure is realized. Furthermore, if $r_A$ decreases, t also does and the lattice structure transforms to the rhombohedral structure ($0.93 < t < 1$) and then to the orthorhombic structure ($t < 0.93$), in which the bending of Mn–O–Mn bond and the deviating of the

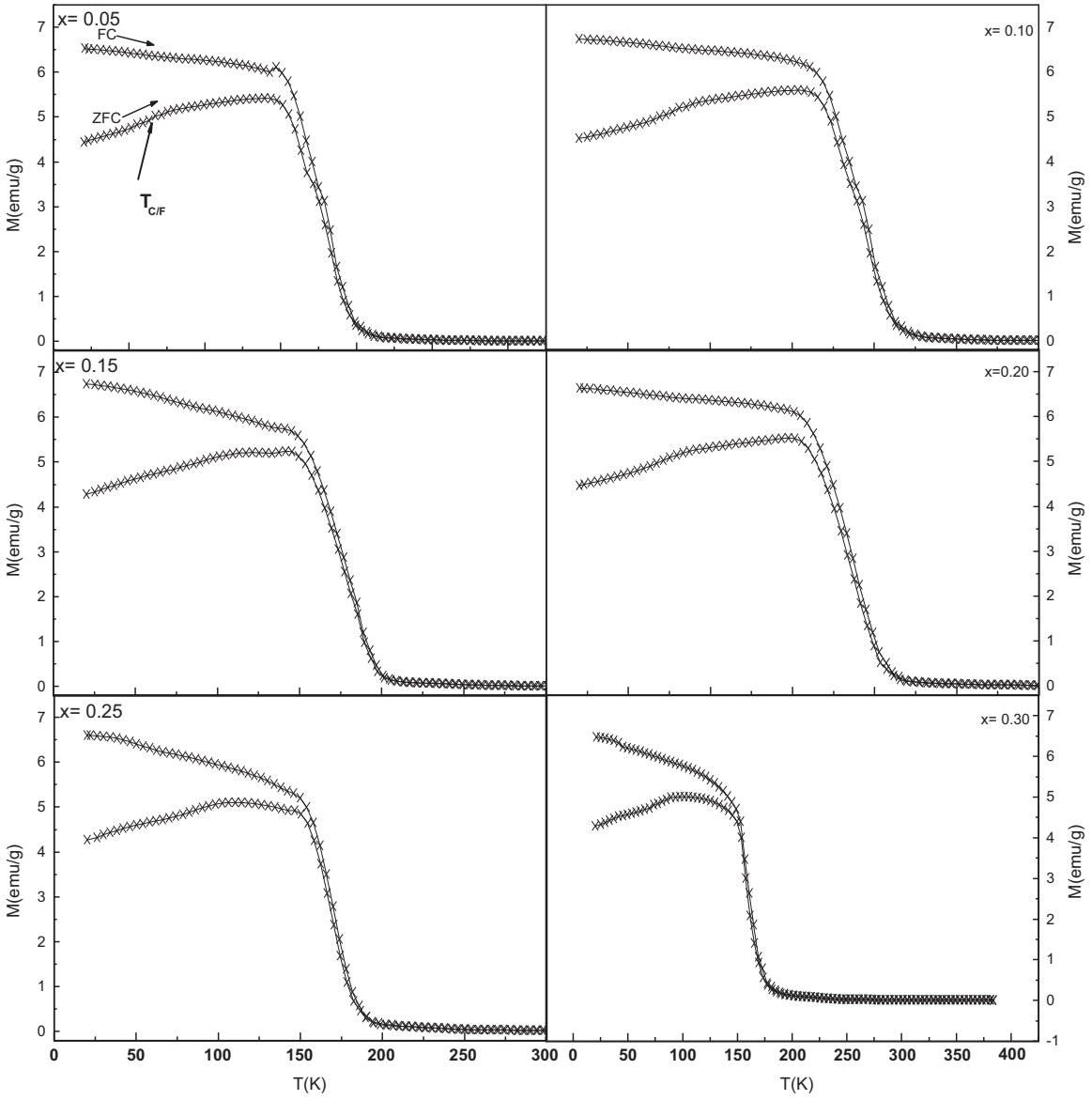


**Fig. 3.** Magnetization vs. temperature curves of $La_{1-x}Li_xMnO_3$ ($x$=0.05–0.30) measured under ZFC and FC condition in a magnetic field of 100 Oe.

bond angle from 180° increase. In these samples the tolerance factor ($t_{calc.}$ and $t_{obs.}$) show a downward trend, resulting in transforming the crystal structure to low symmetry.

Another issue can contribute to the lattice distortion which is the deformation of the $Mn^{3+}O_6$ octahedra originating from the Jahn–Teller (JT) effect that is inherent to the high-spin ($S$=2) $Mn^{3+}$ ions with double degeneracy of the $e_g$ orbital. The static JT distortion is given by the following formula [27]:

$$\sigma_{JT} = \sqrt{\frac{1}{3}\sum\left[(Mn-O)_i - Mn-O\right]^2} \quad (1)$$

where $(Mn–O)_i$ stands for the three independent Mn–O bond lengths and ‹Mn-O› is the average Mn–O bond length. As has been mentioned above, our samples are characterized by rhombohedral ($R\bar{3}c$) structure. Since all three Mn–O distances are equal in the $R\bar{3}c$ phase, the static JT distortion parameter is equal to zero according to Eq. (1). This trend is in agreement with the x-ray data. It can be deduced that, the contributions of the static JT distortions are eliminated and only the crystal structure distortions are responsible for the lattice deformation.

Fig. 2 shows the scanning electron microscope (SEM) images of the fractured surfaces of the $La_{1-x}Li_xMnO_3$ ($x$=0.05, 010, 0.15, 0.20, 0.25 and 0.30) samples. The grains are well connecting with each other and the grain sizes significantly change with increasing the Li content. The XRD results allowed to calculate the average crystallite sizes of the materials using Scherrer's formula, $\langle D\rangle = K\lambda/\beta\cos\theta$, where $\langle D\rangle$ is average particle size, $K$ is a constant (shape factor of 0.89), $\lambda$ is the Cu $K_\alpha$ wavelength, and $\beta$ is the full width at half maxima of the XRD peak. The crystallite sizes are found to be in the range of 54–49 nm. Obviously, the grain sizes observed by SEM are several times larger than those calculated by XRD, which indicates that each grain observed by SEM consists of several crystallites.

### 3.2. Magnetic properties

The temperature dependence of magnetization was studied in zero field $M(T)_{ZFC}$ and field $M(T)_{FC}$ cooling regimes at a fixed applied magnetic field 100 Oe within a temperature rang 50–300 K. The $M(T)_{ZFC}$ plots show that all samples undergo a sharp FM to PM transition at certain temperature $T_C$. The Curie temperature ($T_C$) values are determine by the minimum of the d$M$/d$T$ vs.

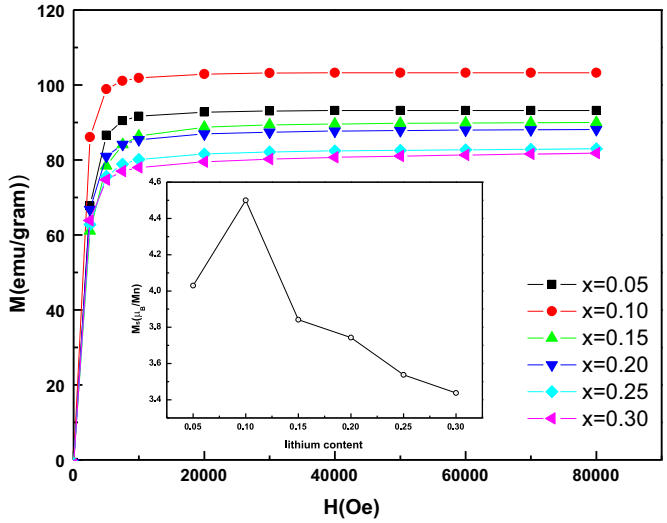


**Fig. 4.** field dependence of the magnetization in $La_{1-x}Li_xMnO_3$ ($x$=0.05–0.) at 5 K is shown. Inset is the variation of the saturation magnetization ($M_s$) vs lithium content.

temperature curves and tabulated in Table 3. In the low doping level (up to $x$=0.10) the $T_C$ values increase as the Li content increase and then decrease with further Li doping. This behavior may be explained by considering the fact that increasing the Li doping raises up the ratio of $Mn^{4+}/Mn^{3+}$ and thus favors the DE interaction. In this process, the number of ferromagnetically aligned domains supersedes the paramagnetically aligned ones so that the percolation threshold is attained and the compound becomes FM, thereby raising the $T_C$ values initially in the low doping regime. As the concentration of $Mn^{4+}$ exceeds $Mn^{3+}$, the SE contribution dominates over DE resulting in a decrease in the $T_C$ values. In fact, similar observations were reported earlier by other groups[28,29]. Furthermore, the transition temperature depends also on the competition between the rhomobedral and orthorhombic phases. Specifically, the rhombohedral perovskite structure is characterized by a weak Hund's coupling favoring an increase in the $T_C$ [30, 31]. In an orthorhombic symmetry, the transfer of the $e_g$ electron is slow when compared with the rhombohedral symmetry. The structural change from rhombohedral to orthorhombic with higher doping may stimulate the corresponding effect.

The low field $M(T)_{ZFC}$ and $M(T)_{FC}$ curves exhibit strong irreversibility just below the $T_C$. Moreover, the ZFC magnetization shows a hump at certain temperature $T_{C/F}$. The $T_{C/F,}$ represents the onset of canting and/or random freezing of the spins, where the magnetization decreases with the decrease of temperature (Fig. 3).

For further clarification, we measured isothermal $M$ vs. $H$ plots at 5 K (Fig. 4). Obviously, the saturation magnetization $M_s$ increases with Li doping up to $x$=0.10 and decreases thereafter (see the inset of Fig. 4). The $M_s$ decrease may be arising from the spin canting [32,33] of the AFM Mn sublattices or existence of local FM regions according to the spin cluster model. It was found that the spin cluster model is more applicable to these magnetic behaviors. It is postulated that the system phase may consists of two separate kinds of clusters depending on the interaction form (direct and/or indirect). The first is the FM clusters characterized by ferromagnetic double exchange interaction between $Mn^{3+}$ and $Mn^{4+}$ while the second is AFM clusters that are embedded in the matrix [32,34–36]. The AFM cluster occurs due to the $Mn^{3+}$–$Mn^{3+}$ or $Mn^{4+}$–$Mn^{4+}$ interactions. The coexistence of and competition between FM and AFM interactions could lead to spin glass (SG)-like behavior. The observed behavior of the $M_s$ can be interpreted similarly as was presented above for the change of the $T_C$. That is, by increasing the Li content up to $x \leq 0.10$, the percentage of the $Mn^{4+}$ increases. Consequently, the DE interaction increases and the percolation threshold is attained and the compound becomes FM, thereby the $M_s$ value enhances. Further doping raises up the concentration of $Mn^{4+}$ over that of $Mn^{3+}$. Therefore, the SE contribution dominates over the DE and thus, the observed decrease of the $M_S$ beyond the samples $x$=0.10 is reasonable.

AC susceptibility measurements are crucial method to confirm spin cluster/glass behavior, complex spin states and phase transition. Fig. 5 shows the temperature dependence of the ZFC ac susceptibility. Both $\chi'$ and $\chi''$ (the in-phase and out-of-phase components, respectively) are measured at 11, 111, 1111, 5111, 9111 Hz. The $\chi'(T)$ plots show small decrease below a certain temperature $T_{cusp.}$ The $T_{cusp}$ has a fixed value and does not change with increasing the frequency-suggesting onset of ferromagnetic ordering. Additionally, shoulders have been observed at lower certain temperature. Noteworthy, the temperatures at which these shoulders appear are frequency dependent. (The inset of the figure shows these shoulders at higher magnified scale)

The $\chi''(T)$ plots are characterized by two maxima $\chi''_{max1}$ and $\chi''_{max2}$ at two different temperatures. Noteworthy, the value of the maximum appears at low temperature $\chi''_{max1}$ decreases with increasing the Li doping level up to $x$=0.10 and increases thereafter. This clearly indicates that the loss or dissipation in the system decreases by Li doping up to $x$=0.10 but increases subsequently. The value and position of the high temperature maximum ($\chi''_{max2}$) are nearly frequency independent. However, $\chi''_{max1}$ shows shifts to higher temperatures as the frequency increases. These behaviors are typical for the cluster-glass features [37–39]. The maximum $\chi''_{max2}$ correspond to the onset of the ferromagnetic ordering, while $\chi''_{max1}$ maximum is associated with freezing of the cluster magnetic moments [40].

Glassy orientation in the spin glasses can be determined by the DC magnetization or low frequency AC susceptibility measurements and it is associated by a memory effect. Noteworthy, the SG phase (ordinary or re-entrant) is featured by pronounced memory behavior, whereas the disordered and frustrated FM phase exhibits little or no memory effect [41]. The primary criterion to predict the SG state for a material is $\delta T_f = \Delta T_f / T_f \Delta(\log_{10} f)$, where $\Delta T_f$ represents the change in the $\chi''_{max1}$ position with the frequency variation. For typical spin glass systems, $\delta T_f$ varies in the range of 0.004–0.018 [42]. The quantity $\delta T_f$ for these samples give values around 0.0044, which are in good agreement with the typical values of the spin glass system.

Eq. (2) (the conventional critical "slow down" of the spin dynamics) is used to describe the spin glass behavior in the systems under study [43,44]:

$$\frac{\tau}{\tau_o} \alpha \left( \frac{T_f - T_{SG}}{T_{SG}} \right)^{-z\nu} \quad (2)$$

where $\tau \alpha f^{-1}$, $T_{SG}$ is the critical temperature for SG ordering (this is equivalent to the $f \rightarrow 0$ value of $T_f$), $z\upsilon$ is a constant exponent, and $\tau_0$ is the characteristic time scale for the spin dynamics. The coincidence with Eq. (2) was tested by plotting ln($f$) as a function of ln ($T_f - T_{SG}/T_{SG}$) as shown in Fig. 6 for the sample $x$=0.05 as an example. The best fit to Eq. (2) is obtained by choosing the value of $T_{SG}$ determined by extrapolation to zero frequency (plot is not presented). The values of $\tau_0$ and $z\upsilon$ are then determined from the intercept and slope, respectively. The extracted parameters should be compared to canonical SG systems where typical values are $z\upsilon \approx 10$ and $\tau_0 \sim 10^{-13}$ S [43,44]. As illustrated in Fig. (7) the data show the expected increase in the $\tau_0$ and $T_{SG}$ values with the Li content up to $x$= 0.10 followed by a decrease thereafter with further doping (in consistent with the ZFC dc magnetization data). These data clearly indicate that the Li incorporation results in

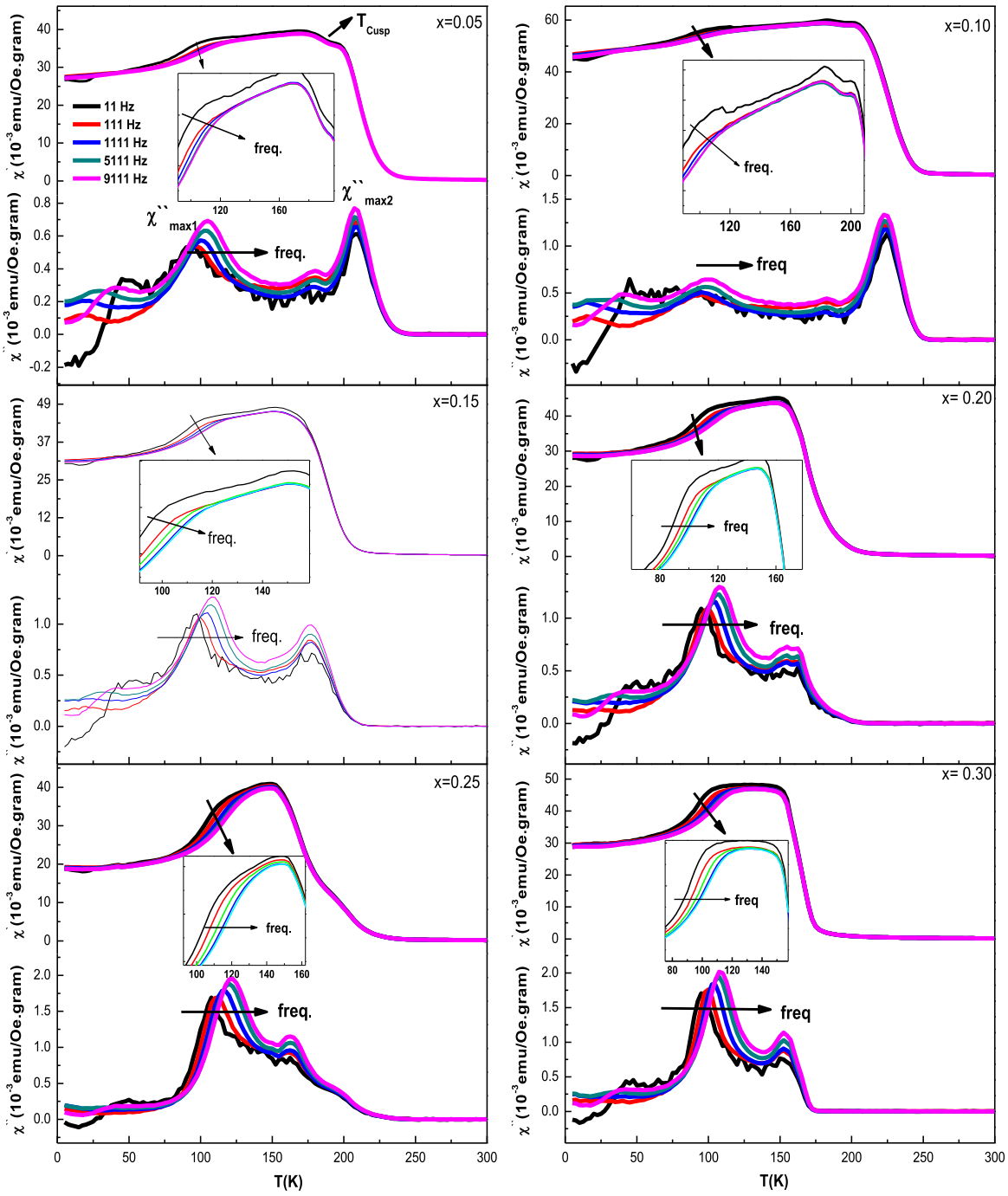


**Fig. 5.** (Color online) temperature dependence of the in-phase $\chi'$ and out–of–phase $\chi'$ and $X''$ components of the ZFC ac susceptibility of $La_{1-x}Li_xMnO_3$ ($x$=0.05–0.30). The data were taken at 11, 111, 1111, 5111, 9111 Hz as indicated in the figure.

slower/faster spin dynamics and larger/smaller cluster sizes in the low/high doping level. The existence of a frequency-dependent peak in $\chi''(T)$ below $T_C$ is a very clear indication that these samples do not exhibit conventional long-range FM ordering.

## 4. Magnetotransport properties

Fig. 8 shows the electrical resistivity vs. temperature $\rho(T)$ plots measured in zero and 0.6 T magnetic field for the $La_{1-x}Li_xMnO_3$ compounds. It was found that, the zero field resistivity increases as the Li content increases. All the compounds exhibit transition from semiconducting state ($d\rho/dT<0$) to a metallic one ($d\rho/dT>0$) on lowering the temperature. The transition occurs at certain temperature values (denoted as $T_{ms}$) which decreases with increasing the Li concentration (as shown in Table 3). Obviously, the low doping is associated with gradual decline of$T_{ms}$.

The observed change of $T_{ms}$ and $\rho$ with both the Li content and crystallite size can be interpreted as the following:

1. The partial substitution of $Li^{1+}$ at A-site ($La^{3+}$) reduces the value of $<r_A>$ (the A-site radius) and thus, increases the variance of the A-cation radius distribution $\sigma^2$ (as shown in Table 1). Therefore, $<r_A>$ becomes too small to fill the space in the cube centers, which makes the oxygen to move towards the centers. Consequently the $(Mn^{3+})$–O–$(Mn^{4+})$ bond bends

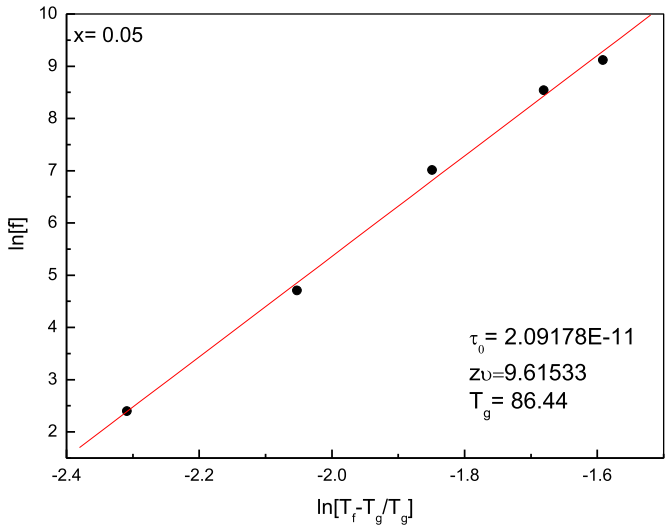


**Fig. 6.** $\ln[(T_f - T_{SG})/T_{SG}]$ for $x=0.05$, demonstrating the agreement with Eq. (2). The solid line is a best fit the data with the parameters shown in the figure.

with a certain angle, act as a local trap for eg electrons, and possibly causes phase or domain separation. Moreover, the transfer integral $b_{ij}$ of the electron hopping decreases as $\Theta$ (Mn–O–Mn) becomes smaller than 180° that leads to deformation of the local lattice in the $MnO_6$ octahedra and in turn influences the double exchange. Consequently, the tendencies of charge localization increases due to the reduction in the carrier mobility and the increase of forbidden band broadness near the Fermi level and thus the electron transport path is blocked.

2. It has been suggest that the rhombohedral structure manganites doped with certain level are characterized by a weak Hund coupling between $e_g$ and $t_{2g}$ spins, and weak electron–phonon coupling that favor an increase in $T_C$ [24,45]. For the samples under investigation, the $T_C$ values increases with the Li concentration $x=0.10$ and thereafter decreases up to $x=0.30$. Therefore, it is logical to predict that Hund coupling and electron–phonon decreases and then increases as the Li content increases.
3. Additionally, Zhang et al. [46] explained the decrease of $T_{ms}$ and the increase of $\rho$ with decreasing the particle size in the view of the core–shell model. The core–shell structure is characterized with enhancement of the grain boundaries and thus higher residual resistivity. Consequently, the density of the ferromagnetic metallic (FMM) particle decreases and the $T_{ms}$ shifts to lower values. Another factor may affect the $T_{ms}$ is the change in the oxygen stoichiometry associated with the tiny size of the crystals.

Regarding the effect of applying magnetic field on the electrical properties of the materials under study, the results imply that applying magnetic field decreases the resistivity of the samples throughout the temperature range. $T_{ms}$ shifts a little to higher temperature side due to alignment of the Mn spins that causes the suppression of the PMS state by FMM state. Because of the spin ordering, the charge carriers also suffer less scattering with increase of the exchange interaction, hence the resistivity decreases, and a large negative magnetoresistance (MR) occurs. Since the spin ordering is more pronounced in the FM phase, the effect of the magnetic field on the resistivity is much more in the low temperature region.

In order to analyze the temperature dependence of MR% plots depicted in Fig. 9, there are two different mechanisms describe the appeared maximum magnetoresistance should be taken in consideration. The first one is the intrinsic magnetoresistance *i*-MR, which arises due to the suppression of spin fluctuations by aligning the spins due to applying of the magnetic field. Note that, the maximum of the *i*-MR appears near the ferromagnetic transition temperature. The second one is the extrinsic magnetoresistance *e*-MR, which arises due to inter-grain spin-polarized

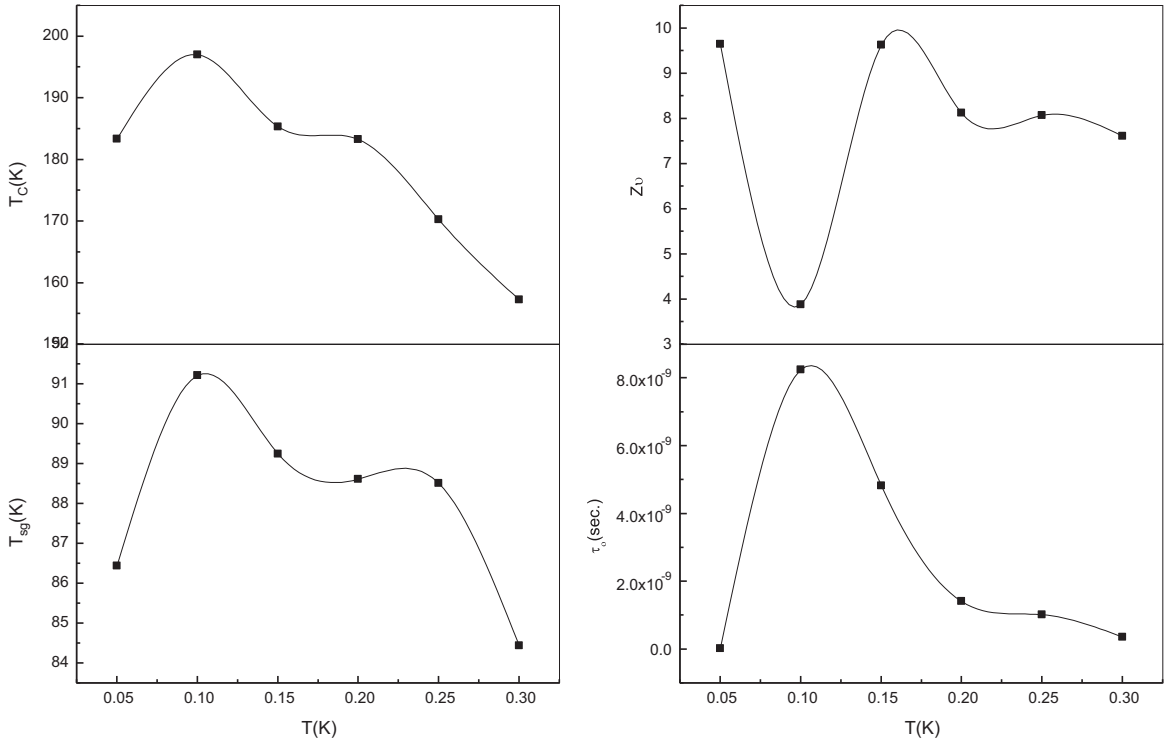


**Fig. 7.** Doping dependence of the Curie temperature ($T_c$), spin-glass temperature ($T_{SG}$), constant exponent ($z\nu$) and relaxation time ($\tau_0$), as extracted from fits of the type shown in Fig. 6.

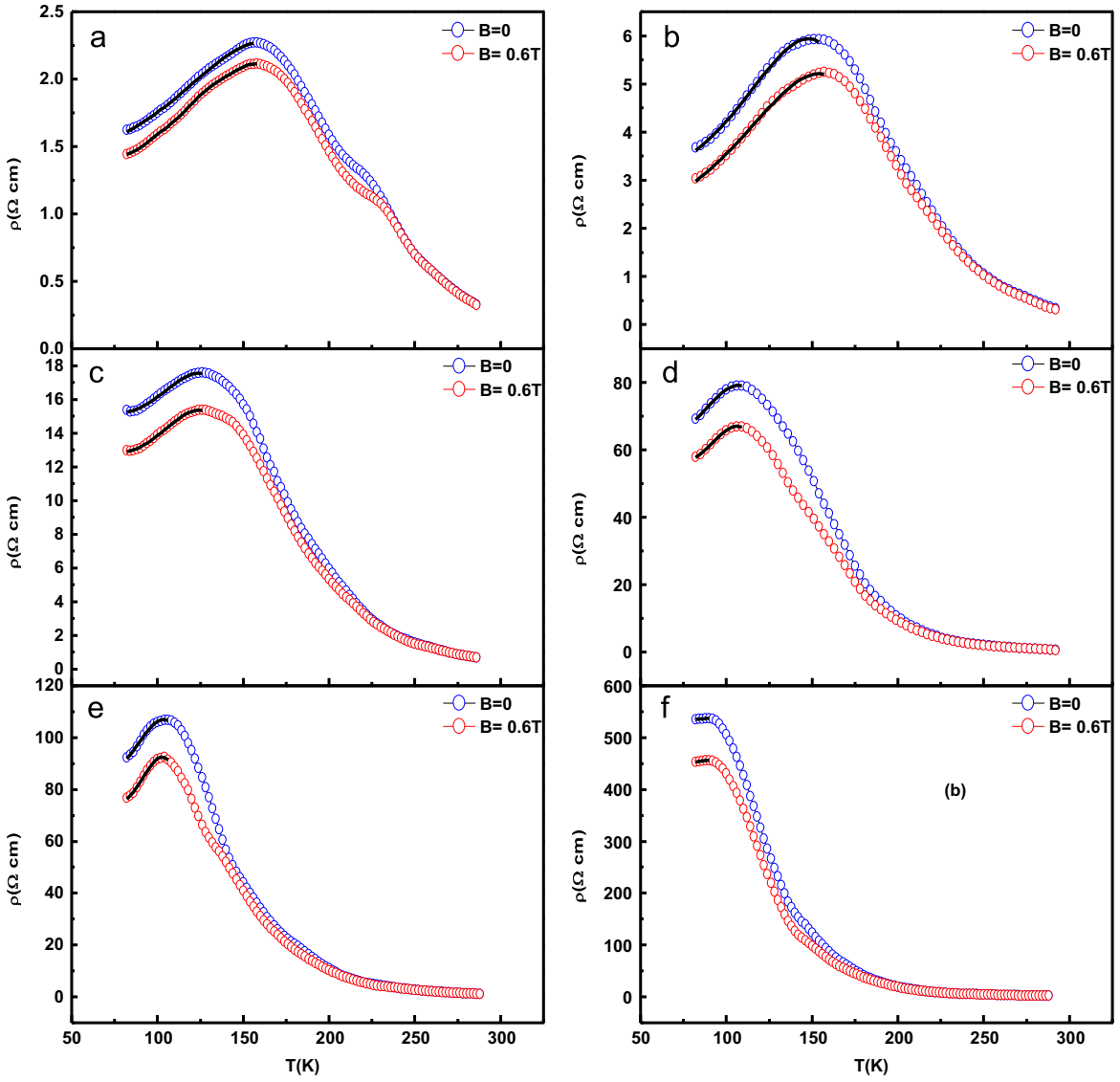


**Fig. 8.** Temperature dependence of resistivity of $La_{1-x}Li_xMnO_3$ ($a-x=0.05$, $b-x=0.10$, $c-x=0.15$, $d-x=0.20$, $e-x=0.25$, and $f-x=0.30$)measured under zero and at an applied magnetic field of 0.6 T. The solid line indicates fit well to Eq. (4).

tunneling across the grain boundaries (GBs) [47–49]. Appearance of the two maxima in the MR–T plots (see Fig. 9), confirm that both mechanisms are strongly effective in the present case. The enhancement of MR% at low temperature is reasonable where the spin polarized tunneling is relatively large due to large disordered surface shells associated to the small size of the particles in our samples.

### 4.1. Conduction mechanism

The low temperature range ($T \leq T_{ms}$) (characterized by FM phase) of the $\rho$–$T$ plots measured with and without magnetic field was found to be well represented by the empirical relation

$$\rho = \rho_0 + \rho_2 T^2 + \rho_{4.5} T^{4.5} \quad (3)$$

where the term $\rho_0$ is the resistivity due to the grain/ domain boundary effects [45,50], $\rho_2 T^2$ term arises due to the electron–electron scattering [51] and the term $\rho_{4.5} T^{4.5}$ arises due to the electron–magnon scattering process [52]. As shown in Table 2, the fitting parameters continuously increase with increasing the dopant amount that is reasonable because of the associated increase of the grain boundaries confirmed above by aforementioned analyses. On the other hand, the alignment of the spins, existed in the domain wall, in the direction of the applied magnetic field and thus improvement of the magnetic domains suppresses various scattering contributions and as a result $\rho_0$, $\rho_2$, and $\rho_{4.5}$ decreases with applying the magnetic field.

The high temperature range ($T \geq T_{ms}$) (characterized by the semiconducting phase) can be divide into two distinct parts described by two different mechanisms. The first one lies in the range $T_{ms} \leq T \leq \theta_D/2$ ($\theta_D$ is the Debye's temperature) and is well described by the variable range hopping (VRH) model proposed by Mott and Davis [53] which includes a hopping of the carriers between states of nearly equal energy. Such states are placed at random distances in the lattice due to the randomness in the potential. Note that, half of the value of $\theta_D$ is defined as the temperature at which deviation from linearity in $\ln(\sigma)$ vs. $T^{-1/4}$ plots occurs. The second part (at $T \geq \theta_D/2$) fits well with the small polaron hopping (SPH) model where the carriers hop only to the nearest neighbors and assisted by the thermal energy. A polaron can be thought to be trapped inside a local energy well of height $E_a$ and, when the field is applied, one side of the well is lowered slightly with respect to the other one, thereby allowing the

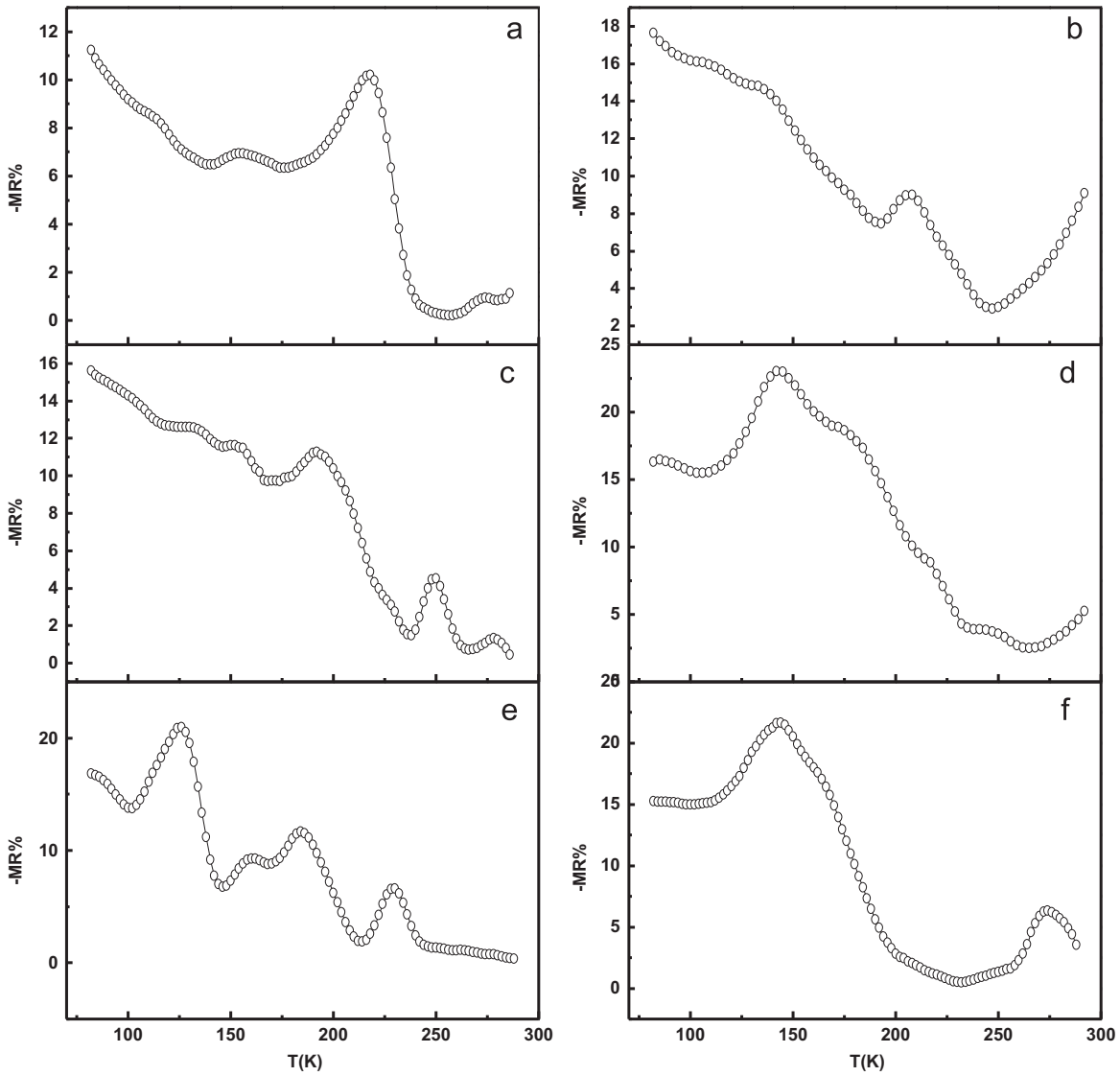


**Fig. 9.** Temperature dependence of Magnetoresistance (MR) of $La_{1-x}Li_xMnO_3$ ($a-x=0.05$, $b-x=0.10$, $c-x=0.15$, $d-x=0.20$, $e-x=0.25$, and $f-x=0.30$) measured at an applied magnetic field of 0.6 T.

**Table 2**
The best-fit parameters obtained from low temperature ($T < T_{ms}$) resistivity data both in presence and in absence of magnetic field for LLMO group of mangnaites.

| Sample | $\rho_0$ (Ω cm) | | $\rho_2$ (Ω cm K$^{-2}$) | | $\rho_{4.5}$ (Ω cm K$^{-4.5}$) | |
|---|---|---|---|---|---|---|
| | $B=0$ T | $B=0.6$ T | $B=0$ T | $B=0.6$ T | $B=0$ T | $B=0.6$ T |
| 0.05 | 1.187353276 | 0.948319177 | 6.35E−05 | 7.34E−05 | −6.02E−11 | −8.26E−11 |
| 0.10 | 1.539861109 | 1.24265431 | 3.19E−04 | 2.68E−04 | −4.44E−10 | −3.35E−10 |
| 0.15 | 12.06705 | 9.540105 | 4.91E−04 | 5.17E−04 | −7.57E−10 | −7.84E−10 |
| 0.20 | 29.19077 | 22.14070822 | 7.48E−03 | 6.61E−03 | −2.63E−08 | −2.27E−08 |
| 0.25 | 50.50192 | 34.11828 | 8.77E−03 | 8.52E−03 | −2.40E−08 | −2.58E−08 |
| 0.30 | 474.3478 | 392.7154 | 1.36E−02 | 1.36E−02 | −7.55E−08 | −7.55E−08 |

polaron to hop easily in that direction [50]. According to the VRH mechanism the temperature dependence of resistivity is represented by the equation,

$$\sigma = \sigma_o \exp\left(-\frac{T_o}{T}\right)^{-\frac{1}{4}} \tag{4}$$

where $\sigma_0$ is a pre-exponential factor, $T_0$ is a constant [$=16\alpha^3/k_B N(E_F)$] and $N(E_F)$ is the density of states at Fermi level which is calculated from the slope of the ln $\sigma$ vs. $T^{-1/4}$ curves (as shown Fig. 10 ). The hopping distance ($R$) and hopping energy ($W$) can be written, at a given temperature $T$, as

$$R = \left[\frac{9}{8\pi\alpha K_B T N(E_f)}\right]^{\frac{1}{4}} \tag{5}$$

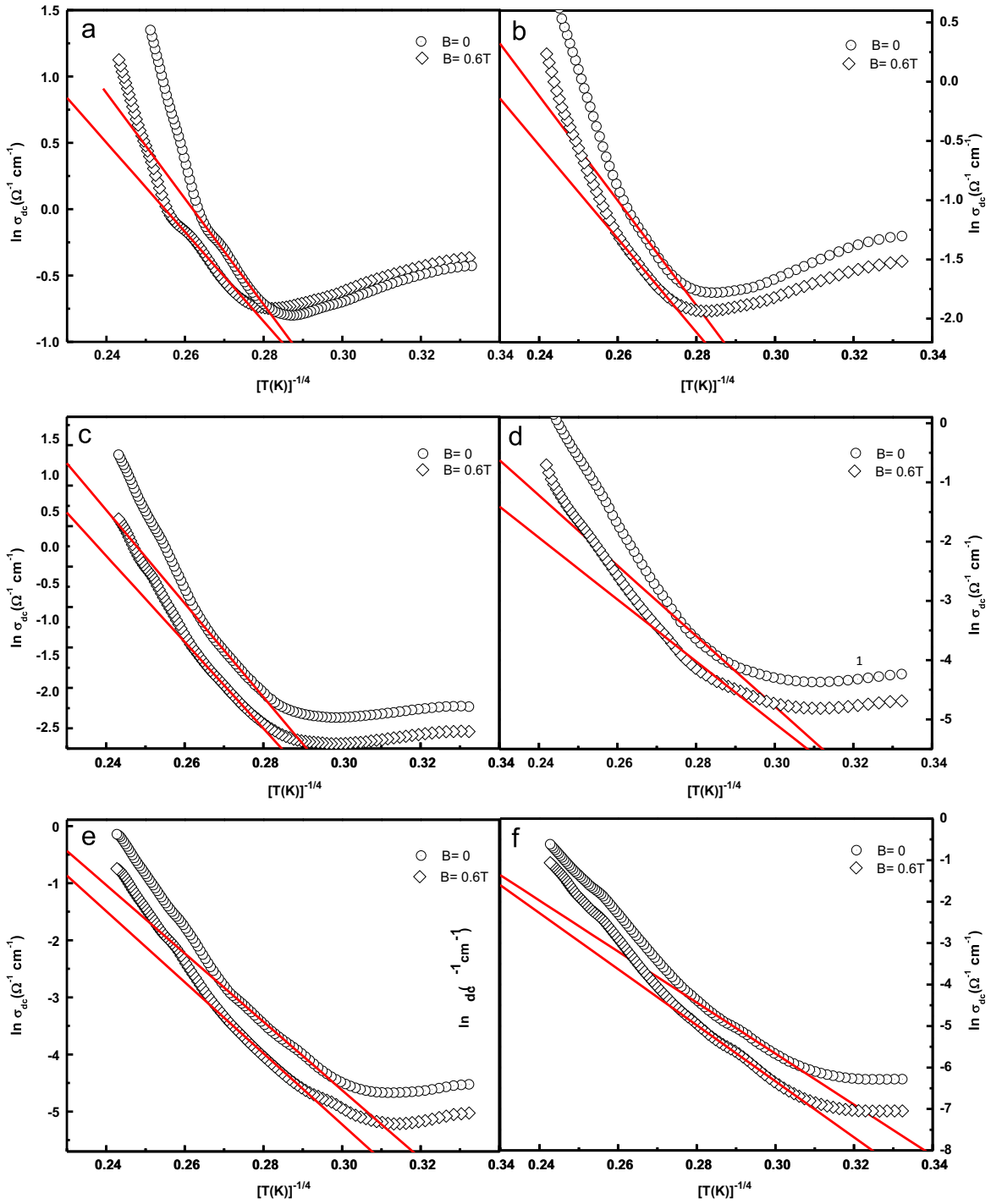


**Fig. 10.** plots of ln($s$) vs. $T^{-1/4}$ of $La_{1-x}Li_xMnO_3$ ($a-x=0.05$, $b-x=0.10$, $c-x=0.15$, $d-x=0.20$, $e-x=0.25$, and $f-x=0.30$) samples. The solid line represents best fit to Eq. (5).

$$W = \left[\frac{3}{4\pi R^3 N(E_f)} W\right] \tag{6}$$

The values of $N(E_F)$, $R$ and $W$ at room temperature were estimated by taking $\alpha = 2.22\ \mathrm{nm}^{-1}$[54] and have been listed in Table 3. Obviously, the calculated values are very close to those reported in other works [55–58]. Additionally, Li doping has significant effect on the calculated parameters where the $T_0$ decreases up to $x=0.10$ and increases thereafter while $N(E_F)$ shows opposite trend. The increase of the $T_0$ value is argued to the following:

- the increase in the bending of the Mn–O–Mn bond and hence the enhancement of the carrier effective mass or narrowing of the band width which in turn results in drastic change in the resistivity and sharpening of the resistivity peak in the vicinity of $T_{ms}$ [59].
- the decrease of the localization length and thus the reduce of the carrier mobility which increases the resistivity and shifts the $T_{ms}$ towards lower temperatures.

**Table 3**
Parameters estimated from the best fit of the electrical transport data using two models.

| Sample | $x=0.05$ | | $x=0.10$ | | $x=0.15$ | | $x=0.20$ | | $x=0.25$ | | $x=0.30$ | |
|---|---|---|---|---|---|---|---|---|---|---|---|---|
| $T_C$ (K) | 183.35 | | 197 | | 185.32 | | 183.27 | | 170.29 | | 157.27 | |
| | $B=0.0$ | $B=0.6$ T | $B=0.0$ | $B=0.6$ T | $B=0.0$ | $B=0.6$ T | $B=0.0$ | $B=0.6$ T | $B=0.0$ | $B=0.6$ T | $B=0.0$ | $B=0.6$ T |
| $T_{ms}$ (K) | 156.000 | 158.000 | 154.000 | 157.000 | 126.000 | 126.000 | 109.000 | 109.000 | 106.000 | 106.000 | 90.000 | 90.000 |
| $\theta_D$ (K) | 460.000 | 468.000 | 416.000 | 422.000 | 412.000 | 424.000 | 362.000 | 368.000 | 360.685 | 368.679 | 356.000 | 376.000 |
| $\nu_{ph}$ (Hz)x$10^{-12}$ | 9.585 | 9.752 | 8.668 | 8.793 | 8.585 | 8.835 | 7.543 | 7.668 | 7.515 | 0.000 | 7.418 | 7.835 |
| $E_\rho$ (meV) | 149.977 | 146.649 | 145.347 | 142.197 | 150.987 | 148.396 | 151.628 | 149.502 | 152.050 | 149.522 | 155.297 | 153.219 |
| $W_H$ (meV) | 145.708 | 142.380 | 141.078 | 137.928 | 146.718 | 144.127 | 147.359 | 145.233 | 147.781 | 145.253 | 151.028 | 148.950 |
| $W_D$ (meV) | 291.417 | 284.760 | 282.155 | 275.856 | 293.436 | 288.254 | 294.717 | 290.466 | 295.563 | 290.506 | 302.056 | 297.900 |
| $H$ (mev) | 30.542 | 30.629 | 28.811 | 28.854 | 28.954 | 29.242 | 27.170 | 27.295 | 27.140 | 27.321 | 27.110 | 27.765 |
| $J$ (meV) | 23.666 | 23.974 | 21.947 | 22.184 | 21.788 | 22.262 | 19.773 | 20.019 | 19.719 | 20.046 | 19.527 | 20.344 |
| $\gamma_p$ | 7.352 | 7.061 | 7.871 | 7.586 | 8.265 | 7.889 | 9.448 | 9.160 | 9.509 | 9.144 | 9.846 | 9.194 |
| exp($\gamma_p$) | 1558.729 | 1165.487 | 2619.794 | 1969.881 | 3885.486 | 2668.473 | 12678.310 | 9504.733 | 13484.277 | 9357.505 | 18884.417 | 9839.073 |
| $T_0$ (K)x$10^{-6}$ | 1.167 | 1.065 | 0.961 | 0.816 | 2.553 | 2.135 | 5.448 | 3.693 | 6.262 | 5.555 | 10.910 | 9.416 |
| $N(E_F)$ ($eV^{-1}cm^3$)x$10^{-20}$ | 17.404 | 19.073 | 21.150 | 24.889 | 7.956 | 9.515 | 3.729 | 5.500 | 3.244 | 3.657 | 1.862 | 2.157 |
| $n$ ($cm^{-3}$)x$10^{-23}$ | 31.725 | 34.768 | 38.553 | 45.370 | 14.503 | 17.344 | 6.797 | 10.026 | 5.914 | 6.666 | 3.394 | 3.933 |
| $R$ (Å)x$10^{-7}$ | 1.388 | 1.356 | 1.322 | 1.269 | 1.688 | 1.614 | 2.040 | 1.851 | 2.112 | 2.049 | 2.426 | 2.339 |
| $W$ (meV) | 51.321 | 50.159 | 48.880 | 46.931 | 62.414 | 59.684 | 75.434 | 68.448 | 78.106 | 75.801 | 89.736 | 86.491 |
| $\alpha R$ | 3.080 | 3.011 | 2.934 | 2.817 | 3.746 | 3.582 | 4.528 | 4.108 | 4.688 | 4.550 | 5.386 | 5.192 |
| $E_s$ (meV) | 50.646 | | 32.494 | | 23.584 | | 21.281 | | 17.611 | | 11.596 | |
| $\alpha$ | −1.802 | | −1.044 | | −0.723 | | −0.601 | | −0.481 | | −0.281 | |

Therefore, The applied magnetic field causes suppression of the magnetic domain scattering, so we found that To values are smaller than in the applied magnetic field [60]. $\upsilon_{ph}$ is known with the optical phonon frequencies which equal to $k_B\theta_D/h$.

Both of $\upsilon_{ph}$ and $\theta_D/2$ decrease as the Li content increases, hence the frequency of the lattice wave decreases. As seen in Table 3 $\theta_D/2$ is much higher than $T_{ms}$, which reveal that the VRH mechanism dominate over a wide range of the temperature of measurements.

At $T \geq \theta_D/2$, the conduction mechanism is described by thermal small polaron hopping [61] and fits well by this model, which it proposed by Mott and Davis [66], viz.

$$\rho/T = \rho_\alpha exp\left(E_\rho/k_BT\right) \tag{7}$$

where $\rho_\alpha$ is the resistivity coefficient, $E_\rho$ is the activation energy and $k_B$ is the Boltzmann constant. The activation energy $E_\rho$ (determined from the slope of the $\ln(\rho/T)$ vs. $1/T$ plots presented in Fig. 11) increases by Li doping with varying $x$ from 0.10 to 0.30 as shown in Table 3. However, it exhibits a decrease with Li doping in the low doping level from $x=$ 0.05 to 0.10. Like this decrease is explained by considering that increasing Li doping level causes charge delocalization and reduce the liberate energy of a free carriers. However, further doping leads to significant increase of the $E_\rho$ value.

On the contrary, while the $E_\rho$ increases. Furthermore, we observed that the activation energies under magnetic field decrease for all doping (Table 3). This is due to delocalization of charge carriers and spin ordering in the system.

For polaron hopping conduction [62]

$$E_\rho = W_H + W_{D/2} (for\ T > \theta_D/2)\ and\ E\rho = W_D\ for\ T < \theta_D/4 \tag{8}$$

where $W_H$ is the polaron hopping energy and $W_D$ is the disorder energy. The difference between $E_\rho$ and $E_s$ (where $E_s$ is activation energy determined from the corresponding temperature range of Seebeck coefficient vs. temperature plots) is the polaron hopping energy; i.e. $W_H$ is determined from the relation [63]

$$W_H = E_\rho - E_s \tag{9}$$

We seek to present a thorough study on the conduction mechanism of the materials, as we try to find out the nature of hopping conduction (adiabatic or non-adiabatic). It is known from Holstien's relation [64] that the polaron bandwidth realize the conditions $J > H$ or $J < H$ for adiabatic or non-adiabatic hopping conduction respectively. Where

$$H = \left(2k_BTW_H/\pi\right)^{1/4}\left(h\nu_{ph}/\pi\right)^{1/2} \tag{10}$$

Note that, the condition should be realized for the small polaron formation is $J \leq W_H/3$ [64]. J can be evaluated from the approximate relation for the high temperature jump site

$$J(T) \approx 0.67h\nu_{ph}(T/\theta_D)^{1/4} \tag{11}$$

The data presented in Table 3 show that $J$ (290 K) $< H$ and $J$ (290 K) $< W_H/3$ which confirm that the DC conduction in the system is due to SPH in non-adiabatic regime. To estimate the small polaron coupling constant ($\gamma$), which is a measure of the electron–phonon interaction constant of the sample, we have used the relation $\gamma = 2W_H/h\nu_{Ph}$ suggested by Mott and Austin [65]. It was found that γ increases as the Li content increases (see Table 3). With applying the magnetic field, $\gamma$ decreases indicating to a decrease in the electron–phonon coupling (and thus causing a decrease of the resistivity). Rao et al. prove that for the La–Na–MnO system $T_{ms}$ increases with the Na doping [66]. They predicted that Na doping induces a transition from strong Hund coupling between $e_g$ and $t_{2g}$ spins to weak Hund coupling. In addition, they argued that the increase of $T_{ms}$ corresponds to a transition from a strong electron–phonon coupling (give rise to a high resistivity) to a weak electron–phonon coupling (favor low resistivity). From the calculation of coupling constant $\gamma$ we deduced that the decrease of $T_{ms}$ with Li doping is associated with increase of $\gamma$. Consequently, this confirms the previous predication that Li doping induces a transition from weak Hund coupling between $e_g$ and $t_{2g}$ spins to strong Hund coupling.

## 5. Thermoelectric power

### 5.1. Low temperature range

In order to study the thermoelectric power (TEP) properties, temperature dependence of Seebeck coefficient (S) measurements were carried out within a temperature range of 80–300 K. The $S$–$T$ plots are depicted in Fig. 12a. The data reveal that Li doping remarkably affects the sign and magnitude of $S$. The samples of $x \geq 0.10$ possess positive $S$ values over the whole range of the

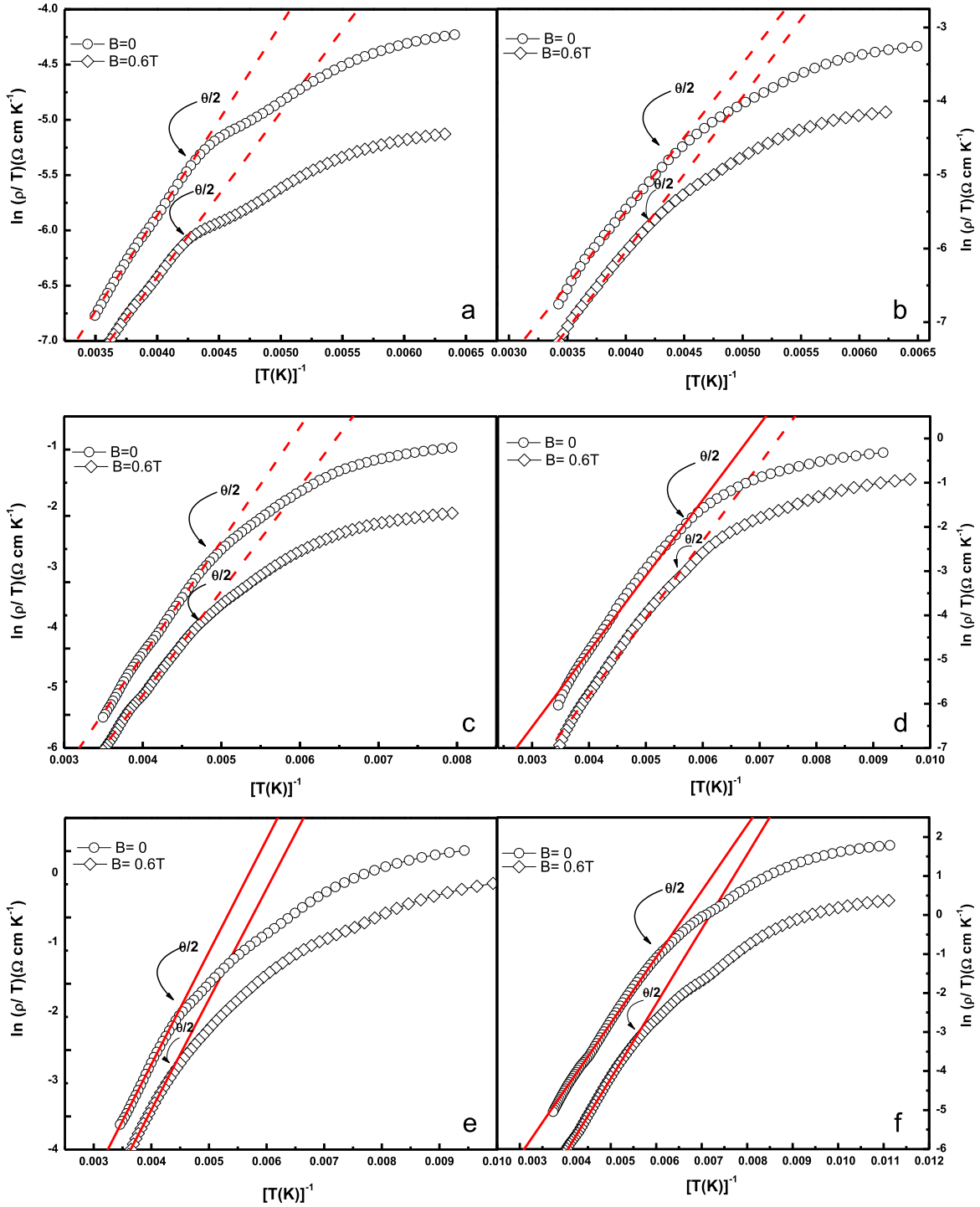


**Fig. 11.** Variation of $\ln(\rho/T)$ vs. $1/T$ of $La_{1-x}Li_xMnO_3$ ($a-x=0.05$, $b-x=0.10$, $c-x=0.15$, $d-x=0.20$, $e-x=0.25$, and $f-x=0.30$) samples. The dash line represents best fit to Eq. (8).

measurement temperature. The sample of the lowest doping level ($x=0.05$) exhibit negative $S$ values at the low temperature range ($T<89$ K) change to positive as the temperature increases to higher values. The change in the $S$ sign may be attributed to the orbital degeneracy of the $e_g$ band. It is well known that the $e_g$ band consists of degenerate 3d orbital (i.e., $d_{3z2\text{-}r2}$ and $d_{x2\text{-}y2}$) and may split into upper and lower bands by an order of $J_H$ [67]. If the lower (spin-up) band splits further into two bands in the FM state then the new lowest band is filled. In such case, the dopants may introduce holes thereby showing positive $S$ values. However if the lowest band still empty; it shows negative (electron-like) values.

All the plots are characterized by a metal–semiconductor transition at certain temperatures denoted as $S(T_m)$ (see Table 4). According to the definition of $S(T_C)$ as the onset temperature of sudden drop of $S$ with increasing the temperature, the values of $T_C$ was determined and tabulated in Table 4. The sudden drop of the $S$ coefficient (as shown in Fig. 12a) may arise from condensation of trapped carriers into (Zener) extended states [63].

Other peaks can be observed at temperatures lower than $S(T_{ms})$ and they appear very common for all manganites. They can be ascribed to either phonon or magnon drag contributions. Therefore, we have analyzed the thermopower data below $S(T_{ms})$ to

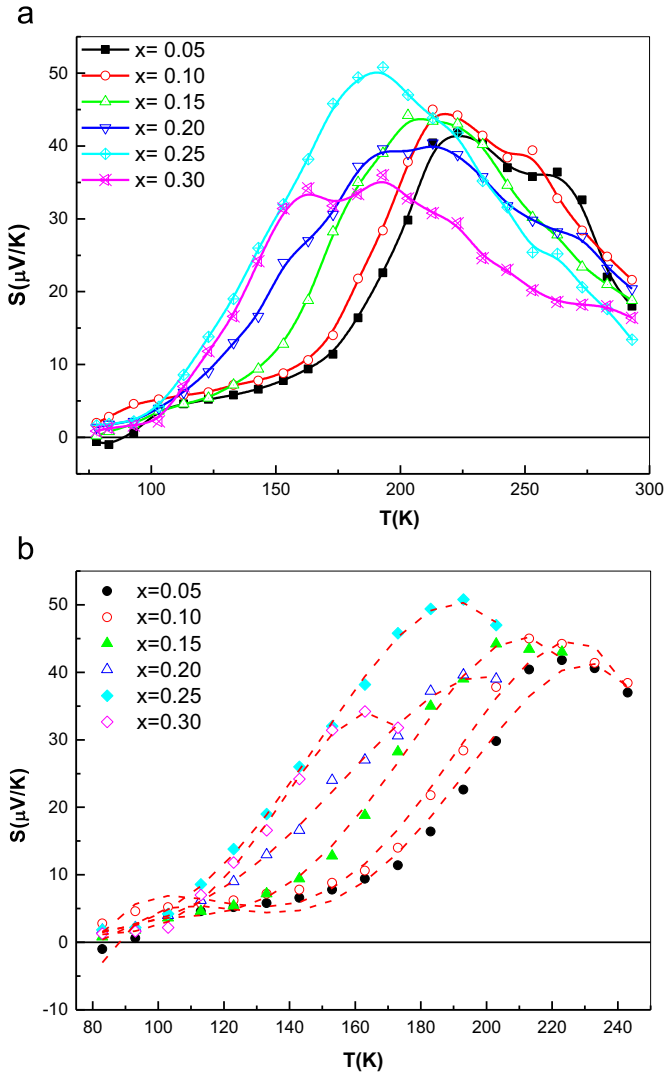


**Fig. 12.** (a) The temperature dependence of TEP from 80 to 300 K. (b) The dash lines represents the fitting with Eq. (14).

explain the origin of lower peak using an expression

$$S = S_0 + S_{3/2}T^{3/2} + S_4T^4 \quad (12)$$

where $S_0$ is a constant which accounts the low temperature variation of thermoelectric power, the second term ($S_{3/2}T^{3/2}$ ) is due to the magnon scattering process and the third term ($S_4T^4$) is attributed to the spin wave fluctuations in the ferromagnetic phase. For our samples, the low temperature data are not well represented with the above equation but fit well with the following equation (see Fig. 13) which takes in consideration the diffusion and phonon drag contribution [68],

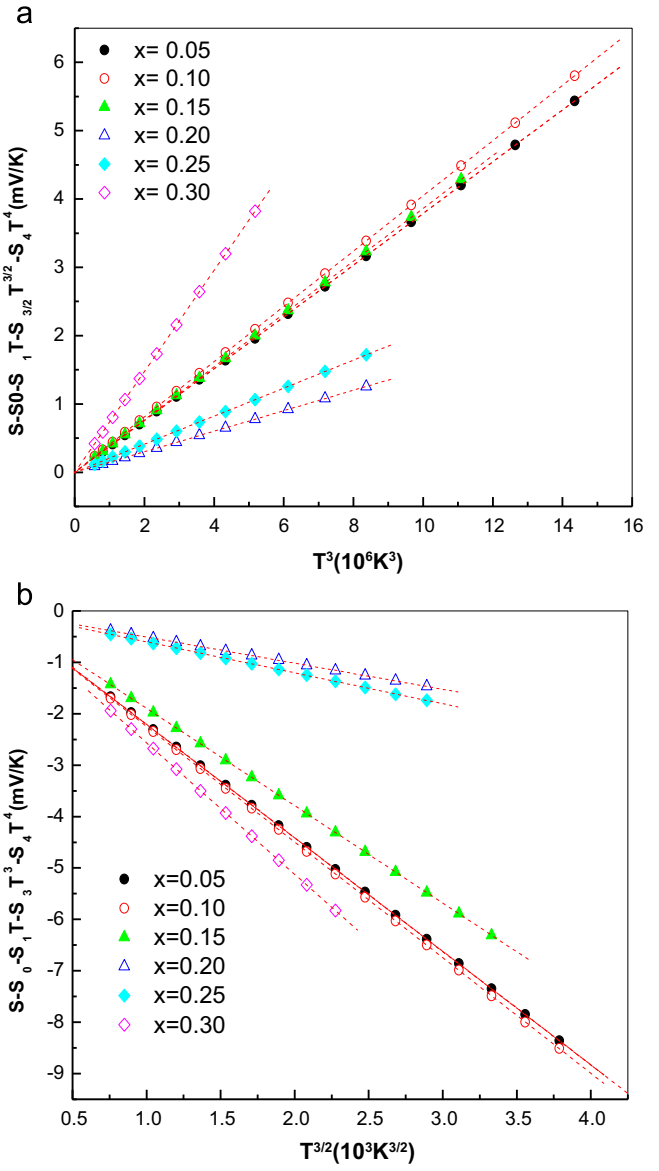


**Fig. 13.** (a) Variation of phonon drag component with $T^3$, and (b) the variation of magnon drag component with $T^{3/2}$.

$$S = S_0 + S_1T + S_{3/2}T^{3/2} + S_3T^3 + S_4T^4 \quad (13)$$

where $S_1T$ and $S_3T^3$ terms are due to diffusion and phonon drag contributions to the thermopower. Table 4 presents the corresponding fitting parameters. Noteworthy, $S_{3/2}$»$S_3$ suggesting strong contribution of electron–magnon scattering at low temperature. It is interesting to note from Fig. 13 that the extrapolated phonon drag component approaches zero as the temperature approaches the absolute zero. This indicates that the phonon drag effect might disappear probably due to depleting the number of phonons at

**Table 4**
The best fit parameters obtained from thermoelectric power data for LLMO3 system.

| Sample | $S$ ($T_{ms}$) | $S$ ($T_C$) | $S_0$ (μV/K) | $S_1$ (μV/K$^2$) | $S_{3/2}$ (μV/K$^{5/2}$) | $S_3$ (μV/K$^4$) | $S_4$ (μV/K$^5$) |
|---|---|---|---|---|---|---|---|
| 0.05 | 283 | 223 | −0.5726 | 2.48E−02 | −2.21E−03 | 3.78E−07 | −7.11E−10 |
| 0.10 | 263 | 213 | −0.55042 | 2.48E−02 | −2.25E−03 | 4.04E−07 | −7.80E−10 |
| 0.15 | 253 | 203 | −0.4186 | 2.01E−02 | −1.89E−03 | 3.88E−07 | −8.14E−10 |
| 0.20 | 243 | 193 | −7.82E-02 | 4.77E−03 | −5.08E−04 | 1.50E−07 | −3.75E−10 |
| 0.25 | 233 | 193 | −7.49E-02 | 5.30E−03 | −6.01E−04 | 2.06E−07 | −5.50E−10 |
| 0.30 | 233 | 163 | −0.4060 | 2.43E−02 | −2.56E−03 | 7.40E−07 | −1.97E−09 |

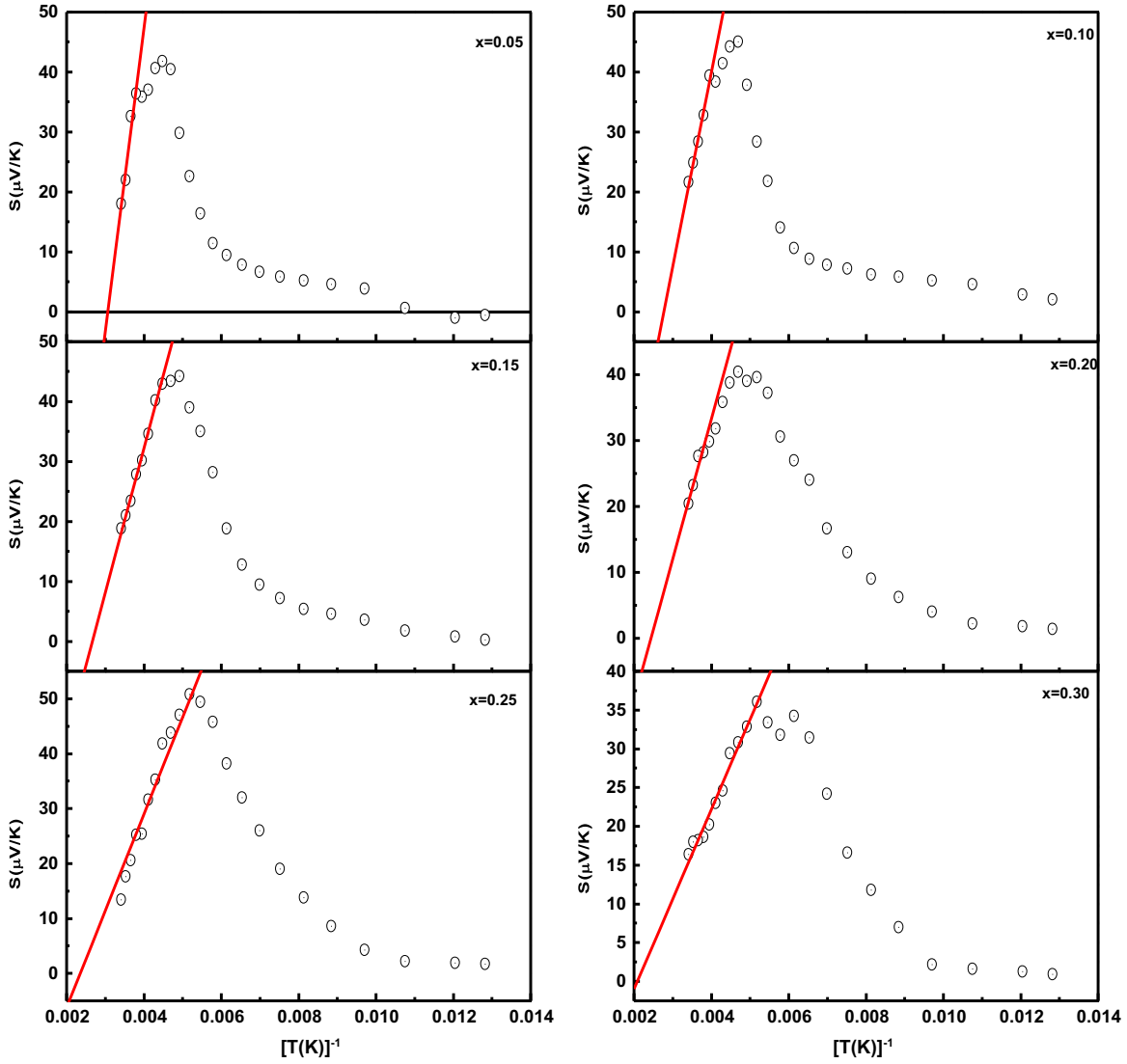


**Fig. 14.** the Variation of $S$ vs. $1/T$ of $La_{1-x}Li_xMnO_3$ samples. The solid line represents the best fit to SPH model.

$T=0$. Furthermore, the overlapping temperatures of the phonon drag are higher than those of the magnon drag indicating that both of them might occurs together in a narrow temperature region. Generally, based on the aforementioned results one can conclude that the magnon and phonon drag effects contribute to the TEP of the samples.

### 5.2. High temperature behavior

The $S(T)$ data at high temperature region (characterized with the paramagnetic/semiconducting phase) fit well with the following equation proposed by Mott [62]:

$$S = k_B/e[E_s/K_BT + \alpha'] \quad (14)$$

where $E_s$ is the TEP activation energy and $\alpha'$ is a constant of proportionality between the heat transfer and the kinetic energy of an electron. $\alpha' < 1$ suggests hopping due to SP and $\alpha' > 2$ suggests existence of large polarons. Coincidence of Mott's equation to our experimental data at high temperature ($T > T_{ms}$) can be obviously observed from the $S$ vs. $T^{-1}$ plots depicted in Fig. 14. The values of $\alpha'$ obtained from intercept of the fitting (Table 3), confirm that the SP hopping characterize the TEP in the paramagnetic region in the materials at hand. As seen in Table 3, the $E_s$ values decrease continuously with the Li concentration. According to the polaron model, the measured activation energy $E_\rho$ is the sum of the activation energy needed for creating the carriers and activating their hopping process, and $E_s$ is the energy required to activate the carriers hopping only. Therefore, the polaron hopping energy ($W_H$) values are calculated using the relation, $W_H = E_\rho - E_s$ and given in Table 4. Note that, large difference between the activation energies $E_\rho$ and $E_s$ is hallmark of the SPH conduction [69]. Note that, the $W_H$ values increase with increasing the Li concentration except in the case of sample $x=0.10$. The increase in the hopping energy signifies a decrease in the polaronic radius ($r_p$) where $r_p$ is inversely proportional to $W_H$ and is given by the relation $W_H = e^2/4\varepsilon(1/r_p - 1/R)$. Therefore, we concluded that the SPH mechanism might be appropriate to explain the electrical resistivity as well as thermopower data in the high temperature regime.

## 6. Conclusion

We have presented a detailed set of structural, magnetotransport, ac susceptibility and thermopower measurements on polycrystallines of $La_{1-x}Li_xMnO_3$ with $x=0.05$–$0.30$ step 0.05. In magnetic properties, the $M(T_C)$ and the magnetization values for

samples of $x \geq 0.10$ are found to decrease with increasing dopant concentration. Clear indications of spin glass a frequency-dependent peak in the in-phase component of ac susceptibility could be observed and described by critical slowing down of spin dynamics. Slower spin dynamics in the low doping level increases and the cluster sizes grow. In terms of magnetotransport properties, we observe and describe the metal to semiconductor transition $T_{ms}$. The magnetoresistance contribution increases as the temperature decreases. Both of intrinsic and extrinsic MR mechanism is strongly effective in the compound. The grain boundary plays a dominant role in the conduction process and it acts as the region of enhanced scattering center for the conduction electron. The thermopower value after an initial increase ($x=0.10$) are found to decrease with increasing dopant concentration and thus also with increasing resistivity. The SPH mechanism might be suitable to explain the electrical resistivity as well as thermopower data in the high temperature regime.

## Acknowledgements

The authors from Sohag University would like to thank Prof Michalis Pissas, Prof Michael Fardis and Prof Vassilis Psycharis for their keen interest in the present work. Also, thank the Greece State Scholarships Foundation (I.K.Y.) for financial support through scholarship.

## References

[1] R. yon Helmot, J. Wecker, B. Holzapfel, L. Schultz, K. Samwer, Phys. Rev. Lett. 71 (1993) 2331.
[2] G.H. Jonker, J.H. van Santen, Physica, 16, (1950) 337.
[3] J.E.O. Wollan, W.C. Koehler, Phys. Rev. 100 (1955) 545.
[4] C. Zener, Phys. Rev. B 82 (1951) 403.
[5] C. Zener, Phys. Rev. 181 (1951) 440.
[6] P.M. Woodward, T. Vogt, D.E. Cox, C.N.R. Rao, A.K. Cheetham, Chem. Mater 11 (1999) 3528.
[7] A.P. Ramirez, J. Phys.: Condens. Matter 9 (1997) 8171.
[8] Q.Y. Xu, R.P. Wang, Z. Zang, Phys. Rev. B 71 (2005) 092401.
[9] H.Y. Hwang, S.W. Cheong, P.G. Radaelli, M. Marezio, B. Batlog, Phys. Rev. Lett. 75 (1995) 914.
[10] L.M. Rodriguez-Martinez, J.P. Attfield, Phys. Rev. B 59 (1999) 13539.
[11] A.J. Millis, P.B. Littlewood, B.I. Shraiman, Phys. Rev. Lett. 74 (1995) 5144.
[12] S. Pal, A. Banerjee, E. Rozenberg, B.K. Chaudhuri, J. Appl. Phys. 89 (2001) 4955.
[13] F.J. Baltt, P.A. Schoreder, C.L. Foiles, D. Gerig, Thermoelectric Power of Metals, Plenum, New York, 1976.
[14] E.M.M. Ibrahim, S.A. Saleh, A.M.A. Hakeem, J. Alloy. Compd. 429 (1) (2007) 19.
[15] P.G. Collins, K. Bradley, M. Ishugami, A. Zettl, Science 287 (2000) 1801.
[16] E.S. Choi, J.S. Brooks, J.S. Qualls, Y.S. Song, Rev. Sci. Instrum. 72 (2001) 2392.
[17] W.,-H. Jung, J. Korean Ceram. Soc. 40 (2003) 849.
[18] P. Mandal, Phys. Rev. B 61 (2000) 14675.
[19] S. Bhattacharya, A. Banerjee, S. Pal, R.K. Mukherjee, B.K. Chaudhuri, J. Appl. Phys. 93 (2003) 356.
[20] A.M. Ahmed, S.A. Saleh, E.M.M. Ibrahim, E. Bontempib, H.F. Mohamed, J. Magn. Magn. Mater. L43 (2008) 320.
[21] A.M. Ahmed, S.A. Saleh, E.M.M. Ibrahim, H.F. Mohamed, J. Magn. Magn. Mater. 301 (2006) 452.
[22] A.M. Ahmed, Physica B 352 (2004) 330.
[23] F.-Y. Shih, K.-Z. Fung, J. Alloy. Compd 391 (2005) 95–103.
[24] G.H. Rao, J.R. Sun, K. Barner, N. Hamad, J. Phys.: Condens. Mater. 11 (1999) 1523.
[25] S. Roy, Y.Q. Guo, S. Venkatesh, N. Ali, J. Phys.: Condens. Mater. 13 (2001) 9547.
[26] R.D. Shannon, Acta Crystallogr. A32 (1976) 751.
[27] X. Xiong, B. Dabrowski, O. Chmaissem, Z. Bukowski, S. Kolesnik, R. Dybzinski, C.W. Kimball, J.D. Jorgensen, Phys. Rev. B 60 (1999) 10186.
[28] C. Shivakumara, M.B. Bellakki, A.S. Prakash, N.Y. Vasanthacharya, J. Am. Ceram. Soc. 90 (2007) 3852.
[29] Y. Moritomo, A. Asamitsu, Y. Tokura, Phys. Rev. B 51 (1995) 16491.
[30] A.J. Millis, B.I. Shraiamn, R. Mueller, Phys. Rev. Lett. 77 (1996) 175.
[31] L. Liu, Y. Liu, J. Miao, Z. Lu, X. Wang, Y. Sui, Z. Liu, Y. Li, Q. Huang, D. Shang, W. Su, J. Alloy. Compd. 427 (2007) 11.
[32] P.G. de Gennes, Phys. Rev. 118 (1960) 141.
[33] G. Matsumoto, J. Phys. Soc. Jpn. 29 (1970) 615.
[34] M. Hennion, et al., Phys. Rev. Lett. 81 (1998) 1957;
M. Hennion, et al., Phys. Rev.B 61 (2000) 9513.
[35] H. Terashita, J.J. Neumeier, Phys. Rev. B 71 (2005) 134402.
[36] N.R. Washburn, A.M. Stacy, J. Phys. Chem. B 104 (2000) 1447.
[37] A. Maihnan, C. Martin, F. Damay, B. Raveau, J. Hei-jtmanek, Phys. Rev. B 54 (1996) 9267.
[38] S. Mukherjee, R. Ranganathan, P.S. Anikumar, P.A. Joy, Phys. Rev. B 54 (1996) 9267.
[39] D.H.N. Nam, K. Jonason, P. Nordblad, N.V. Khiem, N.X. Phuc, Phys. Rev. B 59 (1999) 4189.
[40] E.M.M. Ibrahim, J. Appl. Phys. 113 (2013) 154301.
[41] A.K. Kundu, P. Nordblad, C.N.R. Rao, J. Phys.: Condens. Matter 18 (2006) 4809.
[42] K. Binder, A.P. Young, Rev. Mod. Phys. 58 (1986) 801.
[43] J.A. Mydosh, Spin Glasses: An Experimental Introduction, Taylor & Francis, London, 1993.
[44] K. Gunnarson, P. Svedlindh, P. Nordblad, L. Lundgren, H. Aruga, A. Ito, Phys. Rev. Lett. 61 (1988) 754.
[45] A. Urushibara, Y. Moritomo, T. Arima, A. Asamitsu, G. Kido, Y. Tokura, Phys. Rev. B 51 (1995) 14103.
[46] N. Zhang, W. Ding, W. Zhong, D. Xing, Y. Du, Tunnel-type gian magnetoresistance in the granular perovskite $La_{0.85}Sr_{0.15}MnO_3$, Phys. Rev. B 56 (1997) 8138.
[47] A.-M. Haghiri-Gosnet, J.-P. Renard, J. Phys. D: Appl. Phys. 36 (2003) 127 , R.
[48] A. Gupta, G.Q. Gong, G. Xiao, P.R. Duncombe, P. Lecoeur, P. Trouilloud, Y. Y. Wang, V.P. Dravid, J.Z. Sun, Phys. Rev. B 54 (1996) 15629.
[49] H.Y. Hwang, S.-W. Cheong, N.P. Ong, B. Batlogg, Phys. Rev. Lett. 77 (1996) 2041.
[50] D.C. Worledge, G.J. Snyder, M.R. Beasley, T.H. Geballe, J. Appl. Phys. 80 (1996) 5158.
[51] M. Viret, L. Ranno, J.M.D. Coey, Phys. Rev. B 55 (1997) 8067.
[52] G.J. Snyder, R. Hiskers, S. DiCarolis, M.R. Beasley, T.H. Geballe, Phys. Rev. B 53 (1996) 14434.
[53] N.F. Mott, E.A. Davis, Electronic Processes in Non-Crystalline Materials, Second ed., Clarendon press. Oxford, 1979.
[54] S.L. Ye, W.H. Song, J.M. Dai, K.Y. Wang, S.G. Wang, J.J. Du, J. Appl. Phys. 90 (2001) 2943.
[55] G. Venkataiah, D.C. Krishna, M. Vithal, S.S. Rao, S.V. Bhat, V. Prasad, S. V. Subramanyam, P. Venugopal Reddy, Physica B 357 (2005) 370.
[56] S. Bhattacharya, R.K. Mukherjee, B.K. Chaudhuri, Appl. Phys. Lett. 82 (2003) 4101.
[57] M. Ziese, C.C. Srinitiwarawong, Phys. Rev. B 58 (1998) 11519.
[58] V. Ravindranath, M.S. Ramachandra Rao, G. Rangarajan, Y. Lu, J. Klein, R. Klingeler, S. Uhlenbruck, B. Buchner, R. Gross, Phys. Rev. B 63 (2001) 184434.
[59] J. Fontcuberta, B. Martínez, A. Seffar, S. Piñol, J.L. García-Muñoz, X. Obradors, Phys. Rev. Lett. 76 (1996) 1122.
[60] J.M. de Teresa, M.R. Ibarra, J. Blasco, Phys. Rev. B 54 (1996) 1187.
[61] A.J. Millis, P.B. Littlewood, B.I. Shariman, Phys. Rev. Lett. 74 (1995) 5144.
[62] N.F. Mott, E.A. Davis, Electronic Processes in Non-Crystalline Materials, Clarendon, Oxford, 1971.
[63] J.S. Zhou, W. Archibald, J.B. Goodenough, Nature 381 (1996) 770.
[64] T. Holstien, Ann. Phys. 8 (1959) 343.
[65] N.F. Mott, I.G. Austin, Adv. Phys. 18 (1969) 41.
[66] G.H. Rao, J.R. Sun, K. Bärner, N. Hamad, J. Phys.: Condens. Matter 11 (1999) 1523.
[67] A. Asamitsu, Y. Moritomo, Y. Tokura, Phys. Rev. B 53 (1996) 2952 , R.
[68] B.H. Kim, J.S. Kim, T.H. Park, D.S. Le, Y.W. Park, J. Appl. Phys. 103 (2008) 113717.
[69] S. Battacharya, S. Pal, A. Banerjee, H.D. Yang, B.K. Chaudhuri, J. Chem. Phys. 119 (2003) 3972.